Journal of Atmospheric and Solar–Terrestrial Physics 215 (2021) 105592

Contents lists available at ScienceDirect

Journal of Atmospheric and Solar-Terrestrial Physics

journal homepage: www.elsevier.com/locate/jastp

Climatology and seasonal variation of the thermospheric tides and their response to solar activities over Arecibo

Yun Gong [a,b,*], Xiedong Lv [a,b], Shaodong Zhang [a,b,d,**], Qihou Zhou [c], Zheng Ma [a,b]

[a] School of Electronic Information, Wuhan University, Wuhan, China
[b] Key Laboratory of Geospace Environment and Geodesy, Ministry of Education, Wuhan, China
[c] Electrical and Computer Engineering Department, Miami University, Oxford, OH, USA
[d] State Key Laboratory of Information Engineering in Surveying, Mapping and Remote Sensing, Wuhan University, Wuhan, China

ARTICLE INFO

Keywords:
Atmospheric tides
Thermosphere
Long-term analysis
Incoherent scatter radar

ABSTRACT

A long-term statistical analysis of thermospheric tides in an altitude range from 150 to 400 km is presented. The analysis is based on a dataset with 31 multi-day experiments conducted from an incoherent scatter radar at Arecibo Observatory between 1984 and 2015. This is the first time that the climatological mean and seasonal variations of the thermospheric tides and their response to solar activities are reported using an extensive dataset. The climatological mean amplitude of diurnal tide (DT) is dominant while the amplitudes of the semidiurnal tide (SDT) and terdiurnal tide (TDT) are comparable. Below 250 km, the SDT and TDT phases show downward propagation with vertical wavelengths of 300 and 240 km, respectively. Above 250 km, the DT is the most prominent component except in autumn while the SDT dominates below 250 km except in winter. Above 250 km, the DT is the strongest in winter and its amplitude varies around 28 m/s. Below 250 km, the SDT is prominent in autumn and fluctuates around 35 m/s. The TDT is the most important in winter compared to the other three seasons and its amplitude is slightly less than 20 m/s. The DT and SDT amplitudes show the opposite response to solar activity. Above 250 km, the former increases with increasing solar activity while the latter is the opposite. The enhanced DT amplitude and its phase structure under the high solar activity indicates that the in-situ EUV radiation plays a major role in generating the thermospheric DT over Arecibo.

1. Introduction

Atmospheric solar tides are global-scale oscillations and they are mainly generated by the solar radiation (Chapman and Lindzen, 1970). The periods of the solar tides are related to a solar day, which are 24, 12, 8, and 6 h. The diurnal tide (DT) and semidiurnal tide (SDT) usually have strong horizontal amplitudes and are frequently observed by various instruments (e.g., Forbes, 1995). Comparing to numerous studies on the DT and SDT, the terdiurnal tide (TDT) and quarter-diurnal tide have received less attention due to their relatively small amplitudes and short durations (e.g., Gong and Zhou, 2011; Gong et al., 2018). Owing to their significant impacts on the transportation of atmospheric energy, atmospheric tides have been studied extensively in numerous publications (e.g., Zhou et al., 1997; Huang et al., 2006, 2007; Forbes et al., 2008, 2011; Hagan et al., 1999; Hagan and Forbes, 2002; Oberheide et al., 2007, 2011; Gong et al., 2013; Dhadly et al., 2018; Liu et al., 2019).

Chapman and Lindzen (1970) solved the zonal structure of atmospheric tides and provided a review of the tidal theory. Using numerical models, Forbes (1982a, 1982b) investigated the vertical structure of diurnal and semidiurnal tides in an altitude range from 100 to 400 km. Hagan et al. (1995) established the Global Scale Fluctuation Model (GSWM) that allows users to define important atmospheric parameters such as background wind field, tidal driving force, and dissipation terms. The basic generation mechanisms and characteristics of the migrating solar tides in the mesosphere and lower thermosphere (MLT) region are introduced by Forbes (1995). Hagan et al. (1999) revised the GSWM to predict the migrating solar tide in the troposphere, stratosphere, mesosphere, and lower thermosphere. Hagan and Roble (2001) suggested that non-migrating tides could be excited by nonlinear interaction between migrating tides and planetary waves based on the data obtained from the thermosphere-ionosphere-mesosphere-electrodynamics general

* Corresponding author. School of Electronic Information, Wuhan University, Wuhan, China.
** Corresponding author. State Key Laboratory of Information Engineering in Surveying, Mapping and Remote Sensing, Wuhan University, Wuhan, China.
E-mail addresses: yun.gong@whu.edu.cn (Y. Gong), zsd@whu.edu.cn (S. Zhang).

https://doi.org/10.1016/j.jastp.2021.105592
Received 18 August 2020; Received in revised form 11 November 2020; Accepted 14 February 2021
Available online 27 February 2021

circulation model (TIME-GCM). Using the GSWM, Hagan and Forbes (2002) reported that in the troposphere, non-migrating tides are mainly excited by latent heat release. Based on the self-established numerical tidal model, Huang et al. (2006, 2007) studied the nonlinear interactions on the migrating diurnal and semidiurnal tides.

Aside from numerical studies, extensive observation analyses on atmospheric tides have been reported using ground-based and satellite measurements like meteor radars (e.g., Huang et al., 2013; Yu et al., 2013; Davis et al., 2013), MF radars (e.g., Zhao et al., 2012; Singh and Gurubaran, 2017), Lidars (e.g., Lübken et al., 2011; Fong et al., 2014; Kopp et al., 2015; Baumgarten et al., 2018) and satellites (e.g., Oberheide and Forbes, 2008; Oberheide et al., 2011; Jin et al., 2012; Pancheva et al., 2012; Sakazaki et al., 2012; Moudden and Forbes, 2013; Singh et al., 2018; Liu et al., 2019). The data taken from the Doppler interferometer on board the TIMED satellite allows Oberheide et al. (2007) to report the climatology of nonmigrating semidiurnal tides. Using multi-year observations obtained from meteor radars, Pokhotelov et al. (2018) reported the seasonal variability of atmospheric tides. Liu et al. (2019) presented the vertical structures of the diurnal, semidiurnal, and terdiurnal tides using 15 years' data collected from the Syowa MF radar (69°S, 39°E).

Due to the limitation of detecting instruments, observational studies of atmospheric tides in the altitude range from 120 to 400 km are limited (Oberheide et al., 2011). However, investigating the characteristics of the atmospheric tides in that altitude range is important in understanding the ionosphere-thermosphere system. Above 120 km, incoherent scatter radar (ISR) is an effective instrument to obtain the altitude and time dependence of wind at that altitude range. Using ISR measurements at Millstone Hill (42°N) and St. Santin (45°N), Salah et al. (1975) observed a strong SDT in the altitude range from 100 to 130 km, which is likely excited in the lower atmosphere. Goncharenko and Salah (1998) reported the seasonal and climatological variability of the SDT in the altitude range from 90 to 140 km based on data collected from the Millstone Hill ISR between 1987 and 1997. Using the Arecibo ISR, Harper (1981), Zhou et al. (1997), Gong and Zhou (2011), and Gong et al. (2013, 2018) presented the vertical structure of the atmospheric tides in the thermosphere. Although the Arecibo ISR has been used to study the tidal characteristics in the thermosphere, a statistic and systematic analysis with a long-term dataset is still lacking.

In this study, the climatological mean and seasonal variation of the DT, SDT, and TDT in the thermosphere and their response to solar activities are investigated using the Arecibo ISR experiments conducted between 1984 and 2015. The dataset used in this study and the processing method is described in section 2. The climatological mean and seasonal variation of the thermospheric tides are given in sections 3 and 4, respectively. The response of the thermospheric tides to the solar activities are presented in section 5. Conclusions are summarized in section 6.

2. Data analysis

A dataset with 31 multi-day experiments conducted between 1984 and 2015 using the ISR at the Arecibo Observatory, Puerto Rico (18.3N, 66.7W) is applied in this study. The dates of the dataset and the corresponding geophysical conditions are listed in Table 1. The dataset covers a total of 140 days of measurements and reflects a large variety of geophysical conditions including periods of low, moderate, and high solar activities and different seasons. In this study, we define March, April, and May as spring, June, July, and August as summer, September, October, and November as autumn, and December, January, and February as winter. According to Table 1, the number of experiments in spring, summer, autumn, and winter are 41, 27, 39, and 33 days, respectively, and in low, moderate, and high solar activities are 58, 55, and 27 days, respectively.

The experiments used a multiple radar autocorrelation function (MRACF) program to obtained ion acoustic wave power spectra (Sulzer, 1986). Important ionospheric parameters used in this study including electron temperature, ion temperature, ion drifts, and electron density, which are obtained from the ISR power spectra. The MRACF program measures altitudes from ~150 to ~700 km with a height resolution of ~38 km (Sulzer, 1986). The data-taking techniques using the Arecibo ISR are described in detail by Zhou and Sulzer (1997). Using the ionospheric parameters measured by the Arecibo ISR, neutral winds can be further deduced (Gong et al., 2013). Note that the ratio of ion-neutral collision frequency to the ion gyrofrequency (ρ) is inversely proportional to the zonal wind error. The ion-neutral collision frequency is much smaller than the ion gyrofrequency in the F-region, which results in a very small value of ρ. The zonal wind will be dramatically affected if there is an error in estimating ρ. Hence, the error in the zonal wind is typically too large to be useful in the F-region (Zhou et al., 1997; Gong et al., 2013).

Table 1
Geophysical conditions of the 31 multi-day experiments used in this study.

Experiment number	Dates	$F_{10.7}$ (SFU)	Season
1	Jan.16–19, 1984	93.4–96.6	Winter
2	July 23–25, 1984	85.9–87.3	Summer
3	Sept. 17–22, 1984	73.8–75.9	Autumn
4	Jan. 14–17, 1985	72.3–75.8	Winter
5	Mar. 19–22, 1985	74.2–76.1	Spring
6	Jan. 14–17, 1986	74.4–76.4	Winter
7	Jan. 27–30, 1987	69.8–70.8	Winter
8	Sept. 21–26, 1987	76.4–83.0	Autumn
9	May 30-June 4, 1989	183.0–221.3	Spring
10	Aug. 28–30, 1989	174.1–192.0	Summer
11	Mar. 19–23, 2003	88.3–107.2	Spring
12	Mar. 29-Apr. 3, 2004	107.4–128.3	Spring
13	May 17–20, 2004	107.2–113.7	Spring
14	June 14–18, 2004	103.1–115.1	Summer
15	Nov. 9–13, 2004	93.0–138.1	Autumn
16	Sept. 7–11, 2005	93.6–117.6	Autumn
17	Nov. 17–20, 2005	94.1–99.6	Autumn
18	June 26-July 1, 2006	79.0–89.0	Summer
19	Nov. 24–26, 2008	66.0–66.5	Autumn
20	Jan 18–20, 2010	78.9–81.6	Winter
21	Jan 21–23, 2010	79.8–82.0	Winter
22	Apr. 12–15, 2010	74.9–75.6	Spring
23	Aug. 5–9, 2011	100.2–113.2	Summer
24	Sept. 4–7, 2012	130.0–139.9	Autumn
25	Dec. 11–14, 2012	100.5–115.5	Winter
26	Jan. 8–12, 2013	150.5–168.2	Spring
27	July 8–12, 2013	117.1–124.0	Summer
28	Sept. 27-Oct. 2, 2014	149.3–182.2	Autumn
29	Dec. 16–22, 2014	173.4–208.9	Winter
30	Mar. 17–20, 2015	108.3–113.7	Spring
31	Mar. 20–24, 2015	111.8–132.2	Spring

Many studies have presented detailed derivations of the thermospheric meridional wind using the ISR techniques (e.g., Buonsanto and Witasse, 1999; Santos et al., 2011; Gong et al., 2012). The thermospheric meridional wind can be computed via,

$$u_s = (v_{ap} - v_d) secI \tag{1}$$

where, v_{ap} is the ion drift that anti-parallel to the magnetic field, v_d is the diffusion velocity (positive upward), and I is the dip angle. The diffusion velocity is calculated based on the following equation (e.g., Buonsanto and Witasse, 1999),

$$v_d = -D_a \frac{T_p}{T_r} sinI \left(\frac{1}{n_e}\frac{dn_e}{dz} + \frac{1}{H_p} + \frac{1}{T_p}\frac{dT_p}{dz} + \frac{0.36}{T_r}\frac{dT_r}{dz} \right) \tag{2}$$

where, $D_a = \frac{2k_b T_i}{m_i \nu_{in}}$ is the ambipolar diffusion coefficient with k_b is the Boltzmann constant, m_i is ion mass, T_i is ion temperature; n_e represents electron density;

$H_p = \frac{2k_b T_p}{m_i g}$, $T_p = (T_i + T_e)/2$, $T_r = (T_i + T_n)/2$ with T_e and T_n as electron and neutral temperature, respectively. T_i, T_e, and n_e are

obtained from the ISR measurements. In the F-region, the main ion component is O^+, and its collision frequency with neutral particles is calculated by the following formula (e.g., Buonsanto and Witasse, 1999),

$$\nu_{in} = \frac{k_b\left\{0.3T_r^{0.5}\left(1-0.135log\frac{T_r}{1000}\right)^2[O]+6.7[O_2]+6.9[N_2]\right\}}{519.6\times10^{16}m_{O^+}} \quad (3)$$

where, $[O]$, $[O_2]$, and $[N_2]$ are neutral number densities in cm^{-3}; m_{o+} is the O^+ ion mass in the atomic mass unit. The neutral densities and temperature are adopted from the MSIS-E-90 atm model. Fig. 1 presents the thermospheric meridional wind in the period from 13:00 LT March 29 to 13:00 LT April 3, 2004.

The white area indicates that the data is not available. This is because the electron concentration is very low during the nighttime that the ISR cannot make good measurements (Zhou et al., 1997). The uncertainty of the derivation of the meridional wind is largely due to the O^+-O collision frequency (Gong et al., 2018). The O^+-O collision frequency cannot be directly measured and it has slightly different derivation methods provided by different studies (Joshi et al., 2018 and references therein). As many previous studies (e.g., Buonsanto and Witasse, 1999; Santos et al., 2011; Gong et al., 2012), we adopted the O^+-O collision frequency from Pesnell et al. (1993). Using the same formula of the O^+-O collision frequency, Santos et al. (2011) reported a comparison of the thermospheric meridional wind obtained from the ISR and Fabry-Perot Interferometer at Arecibo. They concluded that the meridional wind obtained from the Arecibo ISR is reliable. A detailed analysis of the O^+-O collision frequency can be found in Joshi et al. (2018). Note that due to large uncertainties of the ambipolar coefficient above 400 km, the meridional wind obtained in this study is limited to the altitude range from ~150 to ~400 km.

The Lomb-Scargle (LS) method (Press et al., 1992) is applied in determining dominant oscillations in the meridional wind. Fig. 2 shows the periodogram of the meridional wind in the period of 13:00 LT March 29 to 13:00 LT April 3, 2004. The LS results larger than 0.006 correspond to confidence levels higher than 95%. As shown in Fig. 2, the diurnal, semidiurnal, and terdiurnal tides are prominent. The DT and SDT dominate at altitudes from 150 to 250 km, while the DT and TDT are the strongest oscillations above 300 km. In order to simultaneously extract the amplitude and phase of the DT, SDT, and TDT, the least square fitting method is used and the fitting formula is:

$$u(t) = DC + A_{DT}\cos(2\pi/24\times t_{LT}) + B_{DT}\sin(2\pi/24\times t_{LT}) + A_{SDT}\cos(2\pi/12\times t_{LT}) + B_{SDT}\sin(2\pi/12\times t_{LT}) + A_{TDT}\cos(2\pi/8\times t_{LT}) + B_{TDT}\sin(2\pi/8\times t_{LT}) \quad (4)$$

where u(t) is the meridional winds, *DC* is the mean background wind, the subscripts of *DT*, *SDT*, and *TDT* represent the diurnal, semidiurnal, and terdiurnal components, respectively, t_{LT} is the local time (i.e., Atlantic Standard Time). The amplitudes and local time of the maximum meridional winds can be derived as follows:

$$Amp = \sqrt{A^2+B^2} \quad (5)$$

$$LT = \frac{\arctan\left(\frac{B}{A}\right)}{2\pi T} \quad (6)$$

where *Amp* is the amplitude of tidal components and *LT* is the local time of maximum meridional wind, *T* is the period of each tidal component. Since 31 multi-day experiments are used, 31 vertical variations of the amplitude and phase of the DT, SDT, and TDT are obtained. The results of tidal amplitudes and phases are averaged according to different seasons and solar activities. As shown in Fig. 1, a large amount of data below 250 km is absent, which affects the results of the least square fitting. Zhou et al. (1997) presented a detailed study of harmonic fitting in the presence of big data gaps. They concluded that if 50% of the data is absent, the fitting error for DT, SDT, and TDT is 13%, 12%, and 10%, respectively.

3. Climatological characteristics

In order to investigate the climatological characteristics of tidal waves in the thermosphere, all the results of the tidal amplitudes and phases are averaged together. The averaged results of the DT (red), SDT (blue), and TDT (orange) are shown in Fig. 3. To describe the variability of the climatological mean tidal amplitudes and phases, the standard deviation of the results is computed and presented as error bars in Fig. 3. The ratio of the standard deviations to the climatological mean tidal amplitudes are 50–70% for the DT, 50–60% for the SDT, and 30–50% for the TDT. The DT amplitude has the largest variation. The variability of the SDT amplitude below 250 km is larger than above 250 km. The amplitude of the DT dominates above 250 km, which is about 20 m/s. The SDT and TDT amplitudes above 250 km are comparable, which are around 15 m/s. Below 250 km, the SDT amplitude is the most prominent and it reaches its maximum of ~33 m/s at ~188 km. The amplitudes of the DT and TDT below 250 km are around 25 m/s and 15 m/s. The results manifest that the TDT is as important as the DT and SDT over Arecibo.

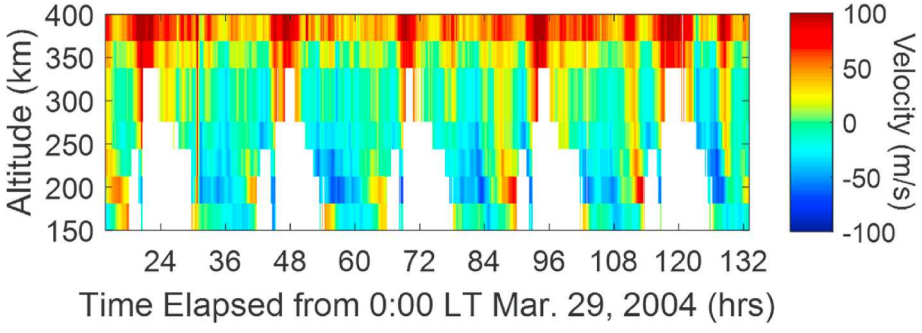

Fig. 1. The variation of the meridional wind in the period of 13:00 LT March 29 to 13:00 LT April 3, 2004.

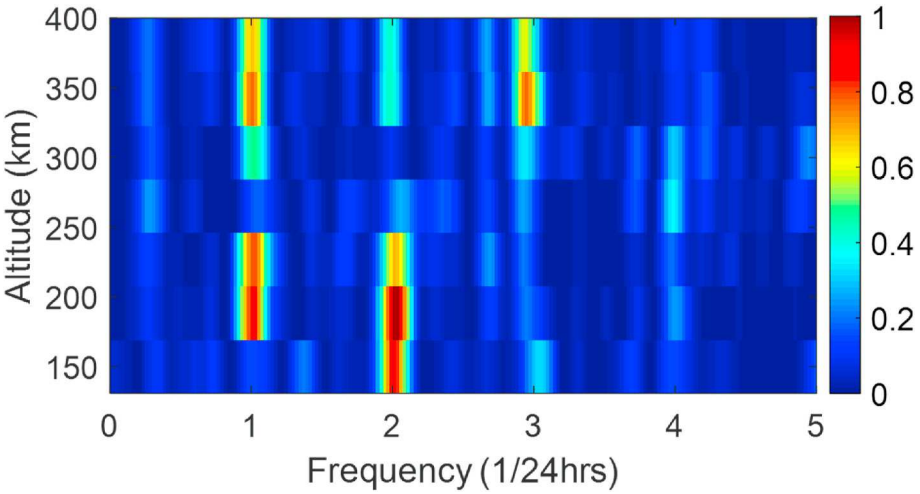

Fig. 2. Normalized Lomb-Scargle periodogram of the meridional wind in the period of 13:00 UT March 29 to 13:00 UT April 3, 2004.

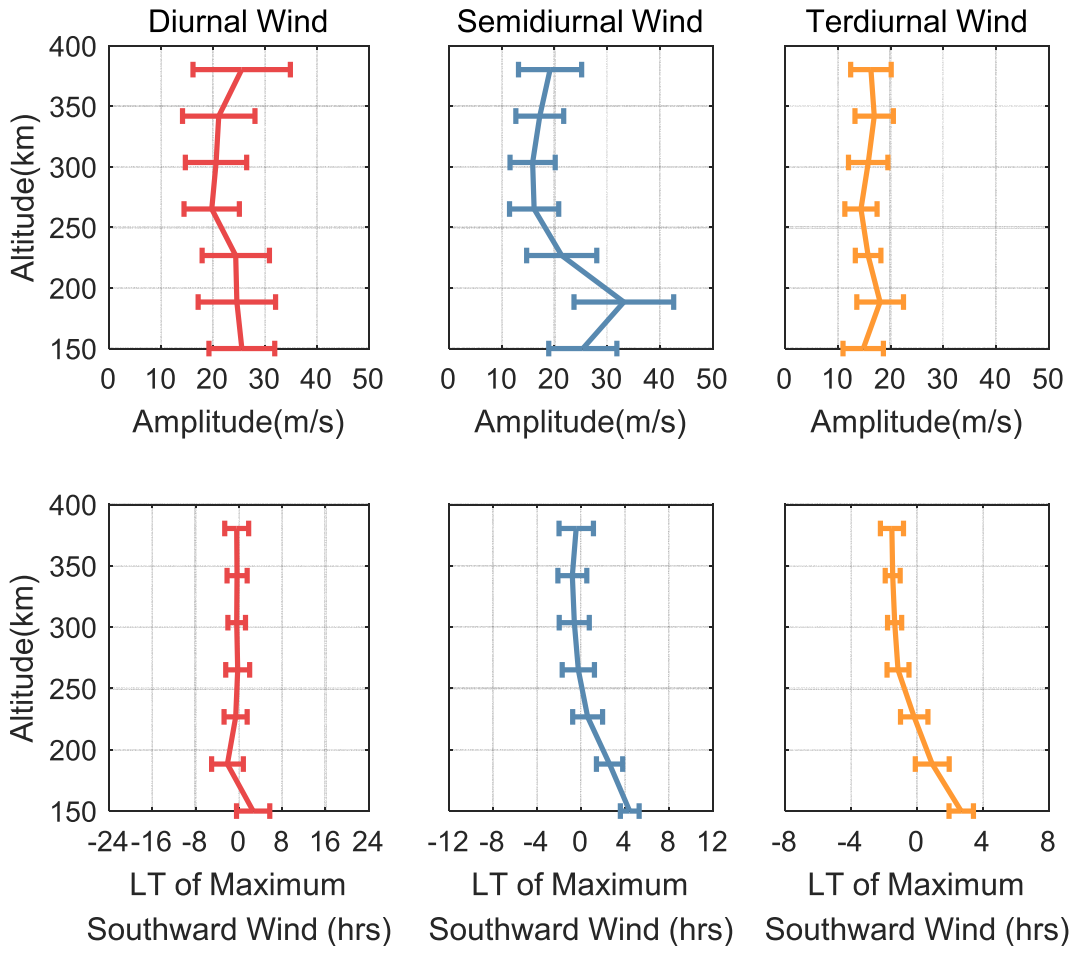

Fig. 3. The climatological mean amplitude (top row) and phase (bottom row) variations of the diurnal (red), semidiurnal (blue), and terdiurnal (orange) tides in the meridional wind. The error bars represent standard deviations.

Like the amplitude, the DT phase has the largest variability as well. The averaged phase variation of the DT, SDT, and TDT is 4.6 h, 2.6 h, and 1.4 h, respectively. The phase of DT above 200 km is largely constant and it varies around 0:00 LT. The phase structure of the DT indicates that the thermospheric diurnal tide is very likely generated by the in situ absorption of EUV radiation. Our results are consistent with a numerical study made by Forbes (1982a). The SDT phase shows limited downward progression above 280 km and the vertical wavelength below 280 km is estimated as 300 km. The phase structure of the SDT below 280 km agrees with the classical $S_{2,\ 2}$ tidal mode (Forbes, 1995). The vertical variation of the TDT phase is very similar to the variation of the SDT phase. The altitude variation of TDT phase is limited and the vertical wavelength of TDT below 280 km is about 240 km. Based on numerical simulations, Forbes (1982a; 1982b) reported that the DT and

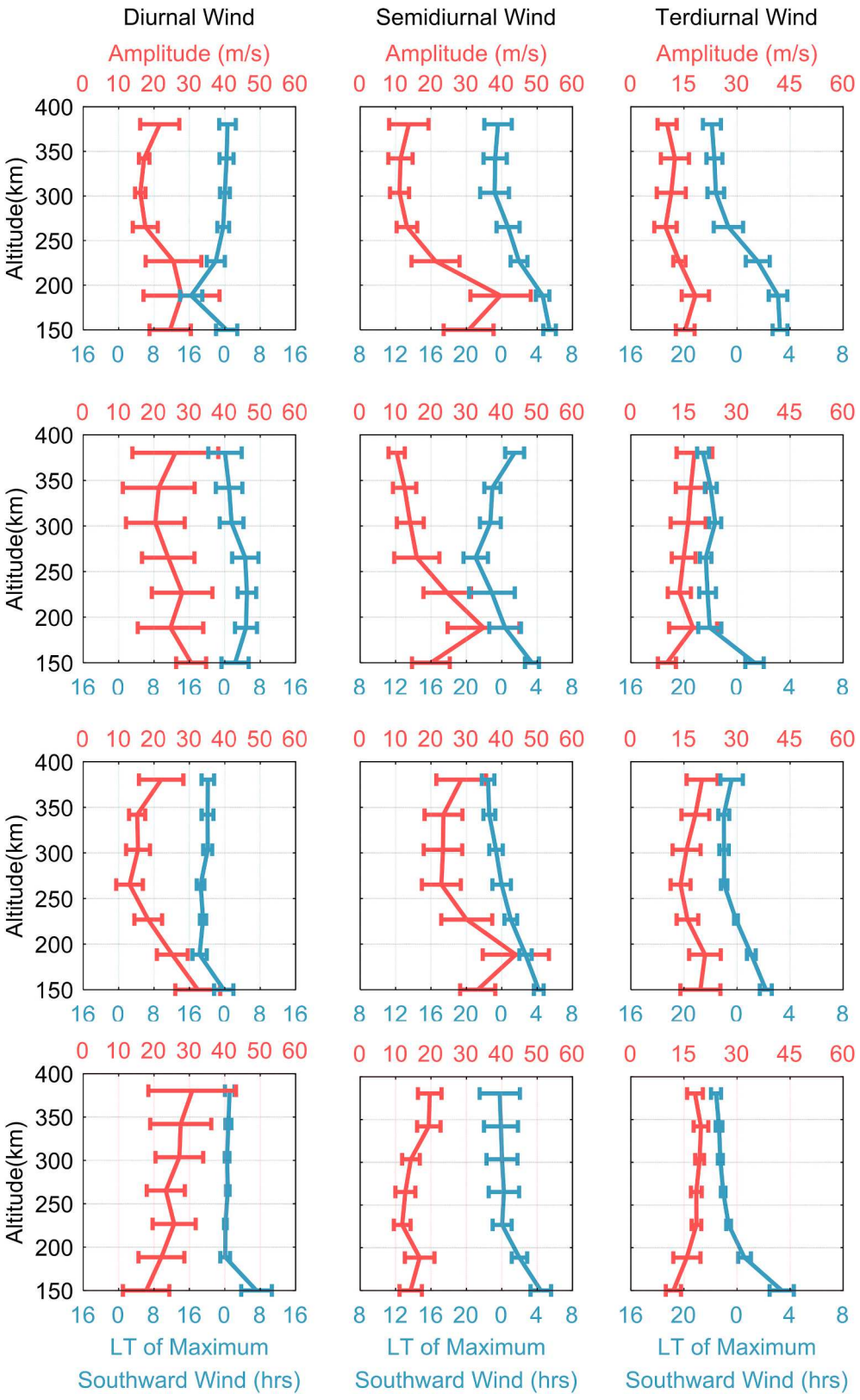

Fig. 4. The vertical variations of diurnal (left), semidiurnal (middle), and terdiurnal (right) tidal amplitudes (red) and phases (blue) in spring (first row), summer (second row), autumn (third row), and winter (fourth row).

SDT phases are largely constant above 200 km. Their results are consistent with our observation of the diurnal component. However, as shown in Fig. 3, the SDT and TDT show clear downward phase propagation below 280 km. Our results indicate that the SDT and TDT excited in the lower atmosphere can propagate upward into higher altitudes than the prediction of the models and the diurnal component.

4. Seasonal variations

The vertical variations of DT (left), SDT (middle), and TDT (right) amplitudes (red) and phases (blue) in spring (first row), summer (second row), autumn (third row), and winter (fourth row) are shown in Fig. 4. The error bars represent the standard deviations. As shown in the first row of Fig. 4, in spring, the amplitudes of the DT is about 15 m/s, which is ~3 m/s larger than the SDT and TDT amplitudes above 250 km. Below 250 km, the SDT is generally larger than the DT and TDT. However, the DT and SDT amplitudes exhibit large variabilities as indicated by the ~20 m/s error bars at around 188 km. Above 250 km, the tidal phases have limited altitude variations. Below 250 km, the SDT and TDT show clear phase propagation and the vertical wavelengths are estimated to be 290 km for the SDT and 160 km for the TDT.

As seen from the second row of Fig. 4, above 250 km in the summer, the DT amplitude, at about 25 m/s, is the largest while the SDT amplitude is the weakest. Below 250 km, the SDT amplitude is dominant. The variabilities of the tidal amplitudes are larger in the summer than in the spring. Above 180 km, the phases of the DT and TDT show litter altitude variation. Below ~270 km, the SDT exhibits a downward phase propagation and the vertical wavelength is about 200 km. Above ~270 km, the SDT phase variation does not change much except at ~380 km. However, since the SDT amplitude is weak (10 m/s) at that altitude, the phase result may not be accurate.

As shown in the third row of Fig. 4, the SDT dominates in autumn, whose amplitude is larger than 22 m/s at all interested altitudes and the maximum value is ~44 m/s. Above 250 km, the DT and TDT amplitudes are comparable at around 15 m/s. The DT and TDT phases are largely constant above 180 and 250 km, respectively. The phase of the SDT shows a downward propagation at all interested altitudes, which is very different from the phase variation in spring and summer.

In winter, as we can see from the fourth row of Fig. 4, the DT amplitude, at ~25 m/s, is the largest among the three tidal components. As in summer, the DT amplitude in winter shows large uncertainties with the error bars larger than 10 m/s at all interested altitudes. In the altitude range from 200 to 350 km, the TDT amplitude is about 5 m/s larger than the SDT amplitude. The phase is largely constant for the DT above 180 km and it has limited altitude variation above 250 km for the SDT and TDT.

According to the results shown in Fig. 4, the DT amplitude is most prominent above 250 km except in autumn while the SDT amplitude dominates below 250 km except in winter. The TDT has the least seasonal variation and its amplitude is the most prominent in winter. Although the TDT is not the largest of the three tidal components in any season, its amplitude is comparable with the DT in autumn and larger than the SDT in winter above 250 km. Our results indicate that the thermospheric TDT is as important as the DT and SDT at Arecibo. The phases of the DT asymptote to constant values above ~250 km in the non-summer seasons. In spring and winter, the DT phases vary around 0:00 LT while the phases in autumn asymptote to around 20:00 LT. In summer, the DT phases show limited variation around 04:00 LT. The

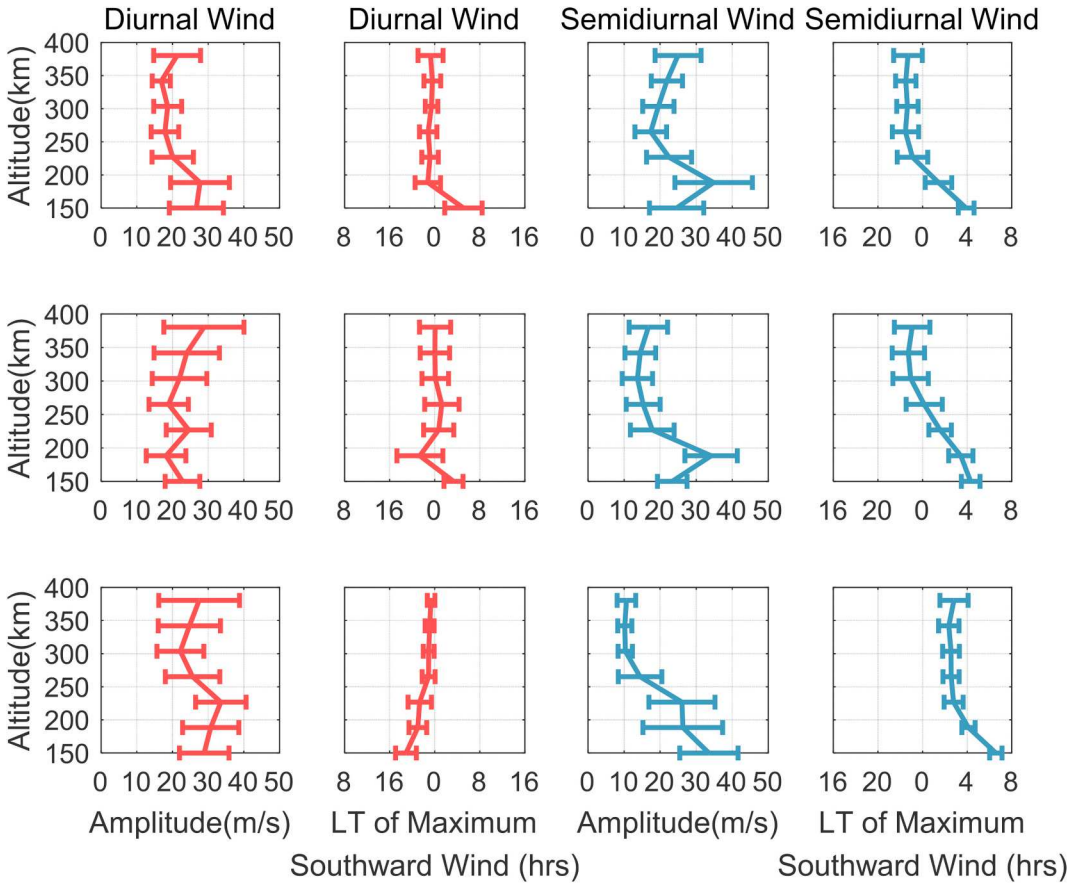

Fig. 5. The amplitude and phase variations of the diurnal (red) and semidiurnal (blue) tides in the meridional wind under the low (F10.7 < 100 solar flux unit (SFU = 10–22 W/m2/Hz), top row), moderate (100 SFU ≤ F10.7 < 140 SFU, medium row) and high (F10.7 ≥ 140 SFU, bottom row) solar activities. The error bars represent standard deviations.

phases of the SDT and TDT show downward phase propagation below 250 km in all seasons. In general, the standard deviations of the tidal amplitudes below 250 km are larger than they are above 250 km.

Using the Arecibo ISR measurements, Harper (1981) reported that the SDT dominates the wind field above 110 km. However, Gong et al. (2013) and Gong et al. (2018) found that the DT is the dominant tidal component in the thermosphere at Arecibo. The inconsistent results in above studies are due to the seasonal differences of atmospheric tides in the thermosphere. The study made by Harper (1981) used the data around equinox while the conclusion made by Gong et al. (2013, 2018) was based on the data collected in winter. According to our observation, in winter, the DT amplitude is the most prominent while the SDT is the weakest among the three tidal components. In autumn, the SDT dominates the meridional wind and the SDT amplitude in spring is larger than the DT amplitude below 200 km.

5. Tidal response to solar activities

The amplitudes and phases of the diurnal (red curve) and semidiurnal (blue curve) components under low (first panel), moderate (middle panel), and high (bottom panel) solar activities in the thermosphere are obtained and presented in Fig. 5. Since the thermospheric terdiurnal tide has a limited response to different solar activities, the results of the TDT are not presented in this paper. As shown in Fig. 5, the DT amplitude increases with increasing solar activity except for the amplitude below 200 km under moderate solar activity conditions. Above 250 km, it appears that the SDT amplitude decreases with increasing solar activity. The phase variation of the DT under the low and moderate solar conditions are very similar, which is different from the variation under the high solar activity below 250 km. In the high solar activity, below 250 km, the DT phase propagates upward as altitude increases, which indicates that the diurnal component propagates downward from 250 to 150 km. Above 280 km, the SDT phases under low and moderate solar activities exhibit little variations at around 22:30 LT while the phases under high solar activity show limited fluctuation around 03:00 LT. There is 3.5 h phase lag between different solar activities.

Amayenc (1974) reported that thermospheric tides are mainly generated via in-situ EUV radiation, dynamo electric field contribution, and tidal waves from the lower atmosphere. Using the theoretical altitude structure of the fundamental symmetric diurnal mode, Amayenc (1974) compared the contributions of the three mechanisms for the thermospheric tides. According to his results, the effect of the in-situ EUV heating results in that the DT phase decreases with decreasing altitudes below 250 km (Fig. 5 in Amayenc, 1974), which is consistent with our results under the high solar activity. It is likely that under the high solar activity ($F_{10.7} \geq 140$ SFU), the in-situ EVU radiation plays a major role in generating the DT in the thermosphere while it is not important in exciting the SDT and TDT at Arecibo.

6. Summary and conclusions

The dataset used in this study consists of 31 multi-day experiments conducted by the Arecibo incoherent scatter radar between 1984 and 2015. The vertical structures of the thermospheric diurnal, semidiurnal, and terdiurnal tides in each experiment are derived. To our knowledge, this is the first time that a long-term statistical analysis of the atmospheric tides in the altitude range from 150 to 400 km has been reported. The climatological mean and seasonal variation of tidal components and their response to solar activities are investigated. New findings are summarized below:

1) The climatological mean DT is the most prominent above 250 km while the climatological mean SDT dominates the other tidal modes below 250 km. The phase of the climatological mean SDT and TDT shows clear downward propagation with a vertical wavelength of 300 km and 240 km in an altitude range from 150 to 280 km, which is different from the model prediction (Forbes, 1982b). Our results manifest that the thermospheric terdiurnal tide is as important as the normally recognized diurnal and semidiurnal tides.
2) Above 250 km, the SDT amplitude is most prominent in autumn while the DT amplitude dominates in the other seasons. Below 250 km, the DT amplitude dominates in winter while the SDT amplitude is generally the largest tidal component in the other seasons. Compared with the DT and SDT, the TDT has the weakest seasonal variations. The TDT in winter is most prominent compared with the other three seasons. Our results reveal that inconsistent statements made by Harper (1981) and Gong et al. (2013, 2018) is due to the seasonal variability of thermospheric tidal waves at Arecibo.
3) Above 200 km, the DT amplitude increases with increasing solar activity while the SDT amplitude decreases with increasing solar activity. The phase of the DT increases as altitude increases below 250 km. Our results may indicate that in-situ EUV radiation plays an important role in the generation of the thermospheric diurnal tide while it is not significant for the excitation of the thermospheric semidiurnal and terdiurnal tides at Arecibo.

Declaration of competing interest

The authors declare that they have no known competing financial interests or personal relationships that could have appeared to influence the work reported in this paper.

Acknowledgments

The Arecibo Observatory is operated by the University of Central Florida under a cooperative agreement with the National Science Foundation. The Arecibo data used here can be obtained from the Madrigal Database at the Arecibo Observatory through http://www.naic.edu/madrigal/index.html/. The F10.7 indexes were downloaded from the SPDF OMNIWeb database (https://omniweb.gsfc.nasa.gov/form/dx1.html). The study is supported by the National Natural Science Foundation of China (through grants 41574142 and 41531070), and the U. S. National Science Foundation grant AGS-1744033.

References

Amayenc, P., 1974. Tidal oscillations of the meridional neutral wind at midlatitudes. Radio Sci. 9 (2), 281–293.
Baumgarten, K., Gerding, M., Baumgarten, G., Lübken, F.J., 2018. Temporal variability of tidal and gravity waves during a record long 10-day continuous lidar sounding. Atmos. Chem. Phys. 18 (1).
Buonsanto, M.J., Witasse, O.G., 1999. An updated climatology of thermospheric neutral winds and F region ion drifts above Millstone Hill. J. Geophys. Res. 104, 24,675–24,687. https://doi.org/10.1029/1999JA900345.
Chapman, S., Lindzen, R.S., 1970. Atmos. Tides. D. Reidel, Norwell, Mass, p. 200.
Davis, R.N., Du, J., Smith, A.K., Ward, W.E., Mitchell, N.J., 2013. The diurnal and semidiurnal tides over Ascension Island (8° S, 14° W) and their interaction with the stratospheric quasi-biennial oscillation: studies with meteor radar, eCMAM and WACCM. Atmos. Chem. Phys. 13 (18), 9543–9564.
Dhadly, M.S., Emmert, J.T., Drob, D.P., McCormack, J.P., Niciejewski, R., 2018. Short-term and interannual variations of migrating diurnal and semidiurnal tides in the mesosphere and lower thermosphere. J. Geophys. Res. Space Phys. 123, 7106–7123. https://doi.org/10.1029/2018JA025748.
Fong, W., Lu, X., Chu, X., Fuller-Rowell, T.J., Yu, Z., Roberts, B.R., McDonald, A.J., 2014. Winter temperature tides from 30 to 110 km at McMurdo (77.8 S, 166.7 E), Antarctica: lidar observations and comparisons with WAM. J. Geophys. Res. Atmos. 119 (6), 2846–2863.
Forbes, J.M., 1982a. Atmospheric tides: 1. Model description and results for the solar diurnal component. J. Geophys. Res. Space Phys. 87 (A7), 5222–5240.
Forbes, J.M., 1982b. Atmospheric tide: 2. The solar and lunar semidiurnal components. J. Geophys. Res. Space Phys. 87 (A7), 5241–5252.
Forbes, J.M., 1995. Tidal and planetary waves. In: Johnson, R.M., Killeen, T.L. (Eds.), The Upper Mesosphere and Lower Thermosphere: A Review of Experiment and Theory, Geophys. Monogr. Ser., vol. 87. AGU, Washington, D. C, pp. 67–87.
Forbes, J.M., Zhang, X., Palo, S., Russell, J., Mertens, C.J., Mlynczak, M., 2008. Tidal variability in the ionospheric dynamo region. J. Geophys. Res. 113, A02310. https://doi.org/10.1029/2007JA012737.

Forbes, J.M., Zhang, X., Bruinsma, S., Oberheide, J., 2011. Sun-synchronous thermal tides in exosphere temperature from CHAMP and GRACE accelerometer measurements. J. Geophys. Res. 116, A11309. https://doi.org/10.1029/2011JA016855.

Goncharenko, L.P., Salah, J.E., 1998. Climatology and variability of the semidiurnal tide in the lower thermosphere over Millstone Hill. J. Geophys. Res. Space Phys. 103 (A9), 20715–20726.

Gong, Y., Zhou, Q., 2011. Incoherent scatter radar study of the terdiurnal tide in the E- and F-region heights at Arecibo. Geophys. Res. Lett. 38 (15).

Gong, Y., Zhou, Q., Zhang, S., Aponte, N., Sulzer, M., Gonzalez, S., 2012. Midnight ionosphere collapse at Arecibo and its relationship to the neutral wind, electric field, and ambipolar diffusion. J. Geophys. Res. 117, A08332.

Gong, Y., Zhou, Q., Zhang, S., 2013. Atmospheric tides in the low-latitude E and F regions and their responses to a sudden stratospheric warming event in January 2010. J. Geophys. Res. Space Phys. 118 (12), 7913–7927.

Gong, Y., Ma, Z., Lv, X., Zhang, S., Zhou, Q., Aponte, N., Sulzer, M., 2018. A study on the quarterdiurnal tide in the thermosphere at Arecibo during the February 2016 sudden stratospheric warming event. Geophys. Res. Lett. 45, 13,142–13,149.

Hagan, M.E., Forbes, J.M., Vial, F., 1995. On modeling migrating solar tides. Geophys. Res. Lett. 22 (8), 893–896.

Hagan, M.E., Burrage, M.D., Forbes, J.M., Hackney, J., Randel, W.J., Zhang, X., 1999. GSWM-98: results for migrating solar tides. J. Geophys. Res. Space Phys. 104 (A4), 6813–6827.

Hagan, M.E., Forbes, J.M., 2002. Migrating and nonmigrating diurnal tides in the middle and upper atmosphere excited by tropospheric latent heat release. J. Geophys. Res. Atmos. 107 (D24). ACL-6.

Hagan, M.E., Roble, R.G., 2001. Modeling diurnal tidal variability with the National Center for Atmospheric Research thermosphere-ionosphere-mesosphere-electrodynamics general circulation model. J. Geophys. Res. Space Phys. 106 (A11), 24869–24882.

Harper, R.M., 1981. Some results on mean tidal structure and day-to-day variability over Arecibo. J. Atmos. Terr. Phys. 43 (3), 255–262.

Huang, C., Zhang, S., Yi, F., 2006. A numerical study on the impact of nonlinear interactions on the amplitude of the migrating semidiurnal tide. Ann. Geophys. 24, 3241–3256.

Huang, C., Zhang, S., Yi, F., 2007. A numerical study on the impact of nonlinearity on the amplitude of the migrating diurnal tide. J. Atmos. Sol. Terr. Phys. 69, 631–648.

Huang, K.M., Liu, A.Z., Lu, X., Li, Z., Gan, Q., Gong, Y., et al., 2013. Nonlinear coupling between quasi 2 day wave and tides based on meteor radar observations at Maui. J. Geophys. Res. Atmos. 118 (19), 10–936.

Jin, H., Miyoshi, Y., Pancheva, D., Mukhtarov, P., Fujiwara, H., Shinagawa, H., 2012. Response of migrating tides to the stratospheric sudden warming in 2009 and their effects on the ionosphere studied by a whole atmosphere-ionosphere model GAIA with COSMIC and TIMED/SABER observations. J. Geophys. Res. Space Phys. 117 (A10).

Joshi, P.P., Waldrop, L.S., Brum, C.G.M., 2018. Ionospheric O+ momentum balance through charge exchange with thermospheric O atoms. J. Geophys. Res. Space Phys. 123, 9743–9761. https://doi.org/10.1029/2018JA025821.

Kopp, M., Gerding, M., Höffner, J., Lübken, F.J., 2015. Tidal signatures in temperatures derived from daylight lidar soundings above Kühlungsborn (54° N, 12° E). J. Atmos. Sol. Terr. Phys. 127, 37–50.

Liu, H., Tsutsumi, M., Liu, H., 2019. Vertical structure of terdiurnal tides in the Antarctic MLT region: 15-year observation over Syowa (69°S, 39°E). Geophys. Res. Lett. 46, 2364–2371. https://doi.org/10.1029/2019GL082155.

Lübken, F.J., Höffner, J., Viehl, T.P., Kaifler, B., Morris, R.J., 2011. First measurements of thermal tides in the summer mesopause region at Antarctic latitudes. Geophys. Res. Lett. 38 (24).

Moudden, Y., Forbes, J.M., 2013. A decade-long climatology of terdiurnal tides using TIMED/SABER observations. J. Geophys. Res. Space Phys. 118 (7), 4534–4550.

Oberheide, J., Wu, Q., Killeen, T.L., Hagan, M.E., Roble, R.G., 2007. A climatology of nonmigrating semidiurnal tides from TIMED Doppler Interferometer (TIDI) wind data. J. Atmos. Sol. Terr. Phys. 69 (17–18), 2203–2218.

Oberheide, J., Forbes, J.M., 2008. Tidal propagation of deep tropical cloud signatures into the thermosphere from timed observations. Geophys. Res. Lett. 35, L04816. https://doi.org/10.1029/2007GL032397.

Oberheide, J., Forbes, J.M., Zhang, X., Bruinsma, S.L., 2011. Climatology of upward propagating diurnal and semidiurnal tides in the thermosphere. J. Geophys. Res. 116, A11306. https://doi.org/10.1029/2011JA016784.

Pancheva, D., Miyoshi, Y., Mukhtarov, P., Jin, H., Shinagawa, H., Fujiwara, H., 2012. Global response of the ionosphere to atmospheric tides forced from below: comparison between COSMIC measurements and simulations by atmosphere-ionosphere coupled model GAIA. J. Geophys. Res. Space Phys. 117 (A7).

Pesnell, W.D., Omidvar, K., Hoegy, W.R., 1993. Momentum transfer collision frequency of O+-O. Geophys. Res. Lett. 20, 1343–1346.

Pokhotelov, D., Becker, E., Stober, G., Chau, J.L., 2018. Seasonal variability of atmospheric tides in the mesosphere and lower thermosphere: meteor radar data and simulations. Ann. Geophys. 36 (3).

Press, W.H., Teukolsky, S.A., Vetterling, W.T., Flannery, B.P., 1992. Numerical recipes in C++. The art of scientific computing 2, 1002.

Sakazaki, T., Fujiwara, M., Zhang, X., Hagan, M.E., Forbes, J.M., 2012. Diurnal tides from the troposphere to the lower mesosphere as deduced from TIMED/SABER satellite data and six global reanalysis data sets. J. Geophys. Res. Atmos. 117 (D13).

Salah, J.E., Wand, R.H., Evans, J.V., 1975. Tidal effects in the E region from incoherent scatter radar observations. Radio Sci. 10 (3), 347–355.

Santos, P.T., Brum, C.G.M., Tepley, C.A., Aponte, N., González, S.A., Robles, E., 2011. Using incoherent scatter radar to investigate the neutral wind long-term trend over Arecibo. J. Geophys. Res. 116, A00H13. https://doi.org/10.1029/2011JA016514.

Singh, D., Gurubaran, S., 2017. Variability of diurnal tide in the MLT region over Tirunelveli (8.7° N), India: consistency between ground-and space-based observations. J. Geophys. Res. Atmos. 122 (5), 2696–2713.

Singh, D., Gurubaran, S., He, M., 2018. Evidence for the influence of DE3 tide on the occurrence of equatorial counterelectrojet. Geophys. Res. Lett. 45 (5), 2145–2150.

Sulzer, M.P., 1986. A radar technique for high range resolution incoherent scatter autocorrelation function measurements utilizing the full average power of klystron radars. Radio Sci. 21 (6), 1033–1040.

Yu, Y., Wan, W., Ning, B., Liu, L., Wang, Z., Hu, L., Ren, Z., 2013. Tidal wind mapping from observations of a meteor radar chain in December 2011. J. Geophys. Res. Space Phys. 118 (5), 2321–2332.

Zhao, L., Chen, J., Ding, Z., Li, N., Zhao, Z., 2012. First observations of tidal oscillations by an MF radar over Kunming (25.6 N, 103.8 E). J. Atmos. Sol. Terr. Phys. 78, 44–52.

Zhou, Q.H., Sulzer, M.P., Tepley, C.A., 1997. An analysis of tidal and planetary waves in the neutral winds and temperature observed at low-latitude E region heights. J. Geophys. Res. Space Phys. 102 (A6), 11491–11505.

Zhou, Q.H., Sulzer, M.P., 1997. Incoherent scatter radar observations of the F-region ionosphere at Arecibo during January 1993. J. Atmos. Sol. Terr. Phys. 59, 2213–2229.